Metal Segregation in Hierarchically Structured Cathode Materials for High Energy Lithium Batteries

Feng Lin,[1] Dennis Nordlund,[2] Yuyi Li,[1] Matthew K. Quan,[1] Lei Cheng,[1,3] Tsu-Chien Weng,[2,†] Yijin Liu,[2,*] Huolin L. Xin[4,*] & Marca M. Doeff[1,*]

1. Energy Storage and Distributed Resources Division, Lawrence Berkeley National Laboratory, Berkeley, CA 94720, USA
2. Stanford Synchrotron Radiation Lightsource, SLAC National Accelerator Laboratory, Menlo Park, CA 94025, USA
3. Department of Materials Science and Engineering, University of California, Berkeley, CA 94720, USA
4. Center for Functional Nanomaterials, Brookhaven National Laboratory, Upton, NY 11973, USA

† Present address: Center for High Pressure Science & Technology Advanced Research, Shanghai 201203, China

Corresponding authors

Y.Liu liuyijin@slac.stanford.edu **H.L.X.** hxin@bnl.gov **M.M.D.** mmdoeff@lbl.gov

Abstract

Controlling surface and interfacial properties of battery materials is key to improving performance in rechargeable Li-ion devices. Surface reconstruction from a layered to a rock salt structure in metal oxide cathode materials is commonly observed and results in poor high-voltage cycling performance, impeding attempts to improve energy density. Hierarchically structured $LiNi_{0.4}Mn_{0.4}Co_{0.2}O_2$ (NMC-442) spherical powders, made by spray pyrolysis, exhibit local elemental distribution gradients that deviate from the global NMC-442 composition; in particular, they are Ni-rich and Mn-poor at particle surfaces. These materials demonstrate improved Coulombic efficiencies, discharge capacities, and high-voltage capacity retention in lithium half-cell configurations. The subject powders show superior resistance against surface reconstruction due to the tailored surface chemistry, compared to conventional NMC-442 materials. This paves the way towards the development of a new generation of robust and stable high-energy NMC cathodes for Li-ion batteries.

Introduction

The development of lithium ion battery technologies has spurred major breakthroughs in portable electronics, power tools, electric vehicles, and grid energy storage. In a lithium ion cell, the energy and power delivery is achieved by shuttling lithium ions between positive and negative electrodes, where the active materials undergo redox reactions using electrons from an external circuit within certain voltage windows. To date, cathode materials have received considerable attention because they are considered to be a primary determinant for increasing cell energy and power densities.[1–4] One way to increase the practical discharge capacities of cathode materials is to increase the upper voltage limit during charge, provided that the electrolytic solution can withstand this increase in cell potential. Side reactions and thermodynamic instability of cathode materials at high voltages (high degree of lithium removal), however, have handicapped this approach. To achieve stable cycling performance for cathode materials, it is important to maintain desirable crystal and electronic structures that allow for efficient transport of electrons and ions for the redox reactions at transition metal sites.[5,6] Numerous studies, in particular those investigated with electronic and structural diagnostic techniques (e.g., core-level spectroscopy, electron microscopy), have shown that undesirable phase transformations occur in cathodes that can lead to failure in batteries cycled to high voltages.[7–14] In particular, surface reconstruction (surface transition metal reduction) from a layered structure to a mixed spinel/rock-salt structure is related to the high-voltage failure of stoichiometric layered cathode materials, i.e., $R\bar{3}m$ $LiNi_{1-x-y}Mn_xCo_yO_2$ (NMC).[7,10,11] In other cathode materials, such as lithium-manganese rich layered NMCs (LMR-NMCs or $xLi_2MnO_3 \bullet (1-x) LiMO_2$ where M=Mn, Ni, Co, etc.), $Li_xNi_{0.8}Co_{0.15}Al_{0.05}O_2$ (NCA) and high-voltage spinel $LiNi_{0.5}Mn_{1.5}O_4$, surface reconstruction is also a factor in the poor Coulombic efficiency, and fast capacity fading that is observed[8,9,15–17] as well as transition metal dissolution and complexation.[18] Our previous DFT calculations indicated that, in NMC materials, the thermodynamic driving force to form rock salt structures increases as a function of the degree of deintercalation.[11,19] Furthermore, it has been shown that cathode-electrolyte side reactions (e.g., simply by exposing NMC materials to $LiPF_6$-based organic electrolytic solutions) also contribute to the surface reconstruction.[12]

Partial substitution (2-4 at%) of Ti on the Co site can improve the stability of NMC materials charged to high voltages because the rock salt formation is delayed to higher states-of-charge compared to the unsubstituted NMC analog.[19–21] Nevertheless, capacity fading in lithium half-cells containing Ti-substituted NMCs cycled to 4.7 V is still evident.[19] Post-mortem analyses of these cells showed the presence of spinel or rock-salt phases on the surfaces of cycled cathode particles.[11,12] Recently, there has been increasing interest in designing interfaces for battery materials, since controlling these interfaces can potentially enable efficient ion and electron transport.[22–25] Forming interfaces between particles can also limit the area of contact between cathode particles and the electrolytic solution and potentially inhibit

undesired side reactions.[12,26] The cycling stability of NMC materials is also governed by the chemical composition, in particular at the surfaces.[27–29] Therefore, the engineering of elemental distribution in NMC ensembles can also potentially improve high-voltage cycling stability. To test these hypotheses, we adopted a scalable spray pyrolysis technique[30–33] to design hierarchically structured NMC powders consisting of large (> 1 μm) spherical particles made up of strongly interfaced nanosized primary particles in which the transition metals are selectively segregated. The resulting materials exhibit excellent resistance against surface reconstruction leading to improved high-voltage electrochemical performance. The present study sets a refined example for optimizing the surface chemistry and morphology of battery materials for vehicular and energy storage technologies.

Results and Discussion

Characterization of NMC materials

Spray pyrolysis was carried out using a homemade system (see Experimental Method).[34,35] The precursor was first prepared by ultrasonically spraying an aqueous solution of mixed metal nitrates through a quartz tube at 700 ºC with air as the carrier gas, and this poorly crystalline powder (see Figure S1 for X-ray diffraction, XRD) was subsequently annealed at 850 ºC for 6 hours in a box furnace. The global chemical composition of the resulting NMC material is very close to the target composition (see Figure S2 for large-area energy dispersive spectroscopy, EDS). Energy resolved transmission X-ray microscopy (TXM)[36–38] was used to determine the distribution of transition metals (i.e., Mn, Co, Ni) in the precursor powder (Figures 1a-1e) and the final $LiNi_{0.4}Mn_{0.4}Co_{0.2}O_2$ (NMC-442) product (Figure 1f-1j). Movies of the 3D elemental distribution are shown in Movies 1 and 2 in the Supporting Information. The representative slices (one voxel thickness, 32.5 nm) through the 3D volume of the hollow microspheres are shown in Figures 1b-1d and 1g-1i. All of the transition metals are present in individual secondary particles, indicating that there was no segregation of elements at the secondary particle level. We then analyzed the elemental association throughout the 3D volume by performing a correlation analysis of the absorption coefficient as a function of the X-ray energies (above and below the K-edges of all the three transition metal elements, see Experimental Method). The Mn-Co-Ni association was only 70% for both the lithium-containing precursor powder and the annealed NMC-442 product. 10% of the total voxels contain a single transition metal in the precursor (Figure 1e), which reduced to 5% after annealing at 850 ºC (Figure 1j). This observation indicates the migration of transition metals during thermal annealing.

Direct visualization was achieved by color mapping individual elemental associations in 3D, as shown in Figure 2. The associated movie of the 3D chemical associations is shown in the Supporting Information (Movie 3). A large number of nanodomains showed significant deviation from the global NMC-442 composition in both the as-made precursor and the annealed NMC particles. There are fewer

three-element domains on the surfaces of the annealed NMC particles compared to the precursor particles (compare Figures 2a and 2c). The interior elemental associations were visualized by slicing through the particles and are shown in Figures 2b and 2d. While the bulks of these particles also deviated from the global NMC-442 composition in parts, there are more three-element domains than on the surfaces for both types of samples. These 3D and 2D elemental association maps clearly show that there is segregation of transition metals throughout the hierarchically structured materials, particularly in the annealed powder and at the surfaces. Metal segregation at similar nanometer scale was also observed previously in lithium-manganese rich layered materials.[39]

The NMC-442 materials are 5-20 μm microspheres that consist of 50-200 nm primary particles (Figure 3a-b), which allows for shorter lithium diffusion distances.[40,41] Although the 3D Ni-Mn-Co association was only 70% (Figures 1 and 2), the resulting NMC-442 material exhibits the expected $R\bar{3}m$ layered structure with approximately 5.6% Li-Ni cation intermixing estimated from the Rietveld refinement (Figure 3c) using the standard NMC-442 $R\bar{3}m$ model, with no evidence of impurity phases in the XRD pattern. In addition, the refined lattice parameters (a=b=2.8708 Å, c=14.2518 Å) are close to those previously reported for NMC materials.[42,43] High-resolution scanning electron microscopy (SEM) imaging shows the primary particles in close contact with one another (Figure 3d). The inter-granular region enclosed by the box in Figure 3d was further studied by aberration-corrected angular dark field scanning transmission electron microscopy (ADF-STEM) and electron energy loss spectroscopy (EELS). Figure 3e shows the ADF-STEM Z-contrast image of the selected area in Figure 3d, where the adjacent particles are perfectly distinguished by the distinct thickness contrasts. In the brighter particle (left) two domains that are π out of phase are projected in this image. The presence of Mn^{4+} and strong transition metal *3d*-oxygen *2p* (TM*3d*-O*2p*) hybridization states are indicative of a pristine $R\bar{3}m$ layered NMC, while in the rock-salt structure commonly observed when surface reconstruction occurs, the transition metals are divalent (e.g., Mn^{2+}) and the hybridization state is much weaker.[9,12,15] EELS scanning was performed across the intergranular boundary along the indicated direction in the selected area (Figure 3e) and spectra were recorded every 90 $Å^2$ (Figure 3f). There were essentially no changes in either O K-edge XAS or Mn L-edge EELS spectra along the scanning pathway. The high TM*3d*-O*2p* hybridization intensity (labeled by purple shade in Figure 3f) is consistent with what is typically reported for pristine $R\bar{3}m$ layered cathode materials.[9,12,15] Therefore, the above characterization at complementary length scales has clearly demonstrated that the resulting materials have the expected $R\bar{3}m$ layered structure. Furthermore, the particle-particle boundary has extremely good coherence, and the bonding environment of cations is not disrupted at the intergranular boundary, as is clearly demonstrated by the STEM-EELS result.

The elemental distribution at the atomic scale also appears to be inhomogeneous. The EELS

spectra were normalized using the Mn L-edge and the evolution of the Co and Ni L-edge intensities were monitored (Figure 4). From the stacked spectra, it is apparent that these do not remain constant along the scanning pathway. To quantify this, we integrated the area of the Ni L_3-edge for each measured area and found that the Ni L_3-integrated area fluctuated along the scanning area (Figure 4b). These observations show that the inhomogeneities are both on an atomic-scale (Figure 4) and on a nanometric scale (Figures 1 and 2).

Electrochemical measurements of NMC materials

The electrochemical performance of the spray-pyrolyzed and annealed NMC-442 was characterized in lithium half-cells. First-cycle coulombic inefficiencies as high as 20% are characteristic of cells containing NMC materials and are observed even after partial charging to voltage limits well below the thermodynamic stability limit of the electrolytic solution.[20,44] The cells containing the spray-pyrolyzed NMC electrodes exhibited much lower first-cycle coulombic inefficiencies than what is typical for unsubstituted NMCs (a maximum of 11.4% when cycled to 4.7 V, Figure 5a) and less charge-discharge polarization than those containing co-precipitated Ti-substituted NMC and combustion synthesized NMC electrodes (Figure S3). The improved efficiencies and reduced polarization result in higher capacities than usual upon the subsequent discharge, particularly for cells cycled to higher voltages (e.g, 228 mAh/g between 2.0 and 4.7 V, compared to 200 mAh/g for the reference material made by combustion synthesis). In fact, the results are similar to those previously reported for Ti-substituted NMC-442 materials, which exhibited improved efficiencies and higher discharge capacities compared to those of unsubstituted NMCs made by combustion synthesis during high-voltage cycling.[20,21] Although capacity fading is still observed for cells containing the spray-pyrolyzed NMC cycled to 4.7 V, retention is better than that of the reference material, even though more capacity is cycled (Figures 5b and 5c), namely, there is a higher degree of lithium intercalation and deintercalation. When the cutoff voltages are decreased to 4.5 V and 4.3 V, the cycling stability of the NMC442 material was significantly improved (Figures 5b and 5c), although the practical discharge capacities were somewhat lower. The effect of changing the lower discharge voltage (Figure 5d) was much less than that of the upper voltage, both in terms of the practical capacity and the capacity retention. The differences between the spray-pyrolyzed and reference samples under this short cycling regime to high potentials are primarily due to the effects of the cathode surface chemistries upon the surface reconstruction phenomena, rather than dendrite formation and side reactions due to electrolytic oxidation, which occur during prolonged cycling.

Investigation of structural stability and surface chemistry

Surface reconstruction from a layered structure to mixed spinel/rock-salt structures, involving the

loss of lithium and oxygen and the reduction of transition metals [7,11] contributes to the failure of NMC materials cycled to high voltages. Since the fraction of surface reconstruction is trivial compared to the bulk in NMC particles, bulk sensitive techniques, such as EXAFS, XRD, and hard XANES, are unlikely to reveal much information about the structural transformation. We have previously established a statistically viable protocol based on high-throughput synchrotron soft X-ray absorption spectroscopy,[11,12] where signals from approximately 10^7 primary particles (estimated using X-ray beam size and primary particle size, 99.97% representing the mean of an infinite ensemble) can be collected at one time. Depending on mode, different sample depths can be accessed; in total electron yield mode (TEY) used for the experiments in Figure 6, the probing depth is about 5-10 nm. Surface reconstruction has also previously been observed on particles removed from cycled cells through STEM/EELS experiments, verifying the soft XAS results.[11] The measurement was performed on composite electrodes containing NMC-442 materials in the discharged state after 20 cycles. The oxidation states of Mn and Co can be used to track the formation of reduced species on particle surfaces for NMCs in the discharged state, consistent with formation of a rock salt phase. However, Ni is divalent in both the discharged NMC-442 layered structure and the rock-salt phase and thus cannot be used to track surface reconstruction. The transition metal L-edge corresponds to the dipole allowed transitions from *2p* to *3d* states, including $2p_{3/2}$ (L_3-edge) and $2p_{1/2}$ (L_2-edge) spin-orbit final states.[45–47] There was no difference between spray-pyrolyzed and co-precipitated NMC-442 materials in the pristine states and the results are consistent with Mn in the tetravalent state and Co in the trivalent state as expected (blue spectra in Figure 6a and 6b).[11] However, low-energy shoulders of Mn L_3- and Co L_3-edges appeared and grew after extended charge-discharge cycles to 4.7 V, indicating an evolution of transition metal *3d* bands to higher occupancies consistent with reduced oxidation states. The reduction of Mn and Co was significantly less severe in the cycled spray-pyrolyzed NMC materials compared to that in the co-precipitated ones, even though more capacity was cycled in the former. This indicates that the spray-pyrolyzed NMC had superior resistance against surface reconstruction (reduction of surface transition metals), which can explain the enhanced high-voltage cycling stability (Figure 5). The cycling stability of NMC materials is clearly affected by the nanoscale transition metal distribution at the surface.[27,28] It is known that nickel-rich cathode materials have a tendency to lose oxygen and to form surface reduced layers, because the unpaired e_{2g} electrons make the high valency nickel ions (e.g., Ni^{3+}) thermodynamically unstable,[48] according to crystal-field theory. To counteract this tendency, compositionally graded cathodes with manganese-rich surfaces have been designed to improve cell safety and cycling characteristics.[27,28] The depth-dependent elemental distribution (calculated using TXM data, Figure 6c) shows that the surfaces (including internal and external surfaces of the subject NMC hollow microspheres) are poorer in nickel and cobalt content and richer in manganese relative to the global NMC-442 composition. The end result of the fortuitous metal

segregation that occurs during processing of the NMC-442 microspheres is less surface reconstruction, leading to improved high-voltage cycling performance. In contrast, in the co-precipitated NMC-442 material (Figure 7), the majority of voxels (more than 90 percent, see the pie chart in panel Figure 7b) in the particle have all the three transition metals, while Co is absent in some of the isolated sub-regions (shown in cyan in Figure 7a), in a random distribution pattern, accounting for only about 7.6 percent of the total volume. The rest of the elemental associations occupy less than 1 percent of the total volume and are, thus, not visible in either Figures 7a or 7b. The depth profile of the elemental concentrations of the studied particle (shown in Figure 7c) also indicates that the co-precipitated particle is relatively more homogeneous than the spray-pyrolyzed one, especially at the secondary particle's surface layer. Therefore, the direct performance and characterization comparisons suggest that the selective metal segregation can indeed deliver higher electrochemical performance.

Conclusion

We have synthesized hierarchically structured $LiNi_{0.4}Mn_{0.4}Co_{0.2}O_2$ (NMC-442) cathode materials consisting of nanoparticles agglomerated into larger spherical secondary particles. The resulting material had the expected $R\bar{3}m$ layered structure with a global composition close to but showed chemical inhomogeneities on both atomic and nanometric length scales. The 3D structural and elemental mapping suggested that the NMC-442 material consists of nanodomains that deviated from the global NMC-442 composition, in particular at the surface regions of the secondary particles, where nickel is depleted. The electrochemical performance measured in lithium half-cells showed superior first-cycle coulombic efficiencies, higher practical discharge capacity and better capacity retention compared to the NMC-442 materials prepared by glycine-nitrate combustion and co-precipitation methods. Mn L-edge and Co L-edge XAS showed that the present NMC-442 material showed superior resistance against surface reconstruction because of the nickel-depleted and manganese-rich surfaces, accounting for the better electrochemical properties. This study indicates that engineering the nanoscale elemental distribution in NMCs may be a fruitful path forward for designing higher energy densities in lithium batteries. From the technological point of view, it is very desirable for the design of energy materials if microscopic techniques with 3D chemical sensitivity at relevant length scales can be applied to investigate the *in operando* behavior of materials in practical environments. The combination of state-of-the-art X-ray and electron microscopy is an excellent candidate for this. However, we would also point out that it is critical to actively develop novel methodologies for reducing the total amount of dose associated with the measurement, to mitigate possible radiation damage.

References

1. Whittingham, M. S. Lithium Batteries and Cathode Materials. *Chem. Rev.* **104,** 4271–4302 (2004).

2. Whittingham, M. S. Ultimate limits to intercalation reactions for lithium batteries. *Chem. Rev.* **114,** 11414–11443 (2014).

3. Doeff, M. M. Batteries: Overview of Battery Cathodes. *Lawrence Berkeley Natl. Lab.* (2011). at <http://escholarship.org/uc/item/1n55870s>

4. Xu, X., Lee, S., Jeong, S., Kim, Y. & Cho, J. Recent progress on nanostructured 4V cathode materials for Li-ion batteries for mobile electronics. *Mater. Today* **16,** 487–495 (2013).

5. Hwang, B. J., Tsai, Y. W., Carlier, D. & Ceder, G. A Combined Computational/Experimental Study on LiNi 1/3 Co 1/3 Mn 1/3 O 2. *Chem. Mater.* **15,** 3676–3682 (2003).

6. Islam, M. S. & Fisher, C. A. J. Lithium and sodium battery cathode materials: computational insights into voltage, diffusion and nanostructural properties. *Chem. Soc. Rev.* **43,** 185–204 (2014).

7. Jung, S.-K. *et al.* Understanding the Degradation Mechanisms of LiNi 0.5 Co 0.2 Mn 0.3 O 2 Cathode Material in Lithium Ion Batteries. *Adv. Energy Mater.* **4,** 1300787 (2013).

8. Xu, B., Fell, C. R., Chi, M. & Meng, Y. S. Identifying surface structural changes in layered Li-excess nickel manganese oxides in high voltage lithium ion batteries: A joint experimental and theoretical study. *Energy Environ. Sci.* **4,** 2223 (2011).

9. Hwang, S. *et al.* Investigation of Changes in the Surface Structure of Li x Ni 0.8 Co 0.15 Al 0.05 O 2 Cathode Materials Induced by the Initial Charge. *Chem. Mater.* **26,** 1084–1092 (2014).

10. Lin, F. *et al.* Influence of synthesis conditions on the surface passivation and electrochemical behavior of layered cathode materials. *J. Mater. Chem. A* **2,** 19833–19840 (2014).

11. Lin, F. *et al.* Surface reconstruction and chemical evolution of stoichiometric layered cathode materials for lithium-ion batteries. *Nat. Commun.* **5,** 3529 (2014).

12. Lin, F. *et al.* Profiling the Nanoscale Gradient in Stoichiometric Layered Cathode Particles for Lithium-ion Batteries. *Energy Environ. Sci.* **7,** 3077–3085 (2014).

13. Yang, F. *et al.* Nanoscale Morphological and Chemical Changes of High Voltage Lithium-Manganese Rich NMC Composite Cathodes with Cycling. *Nano Lett.* **14,** 4334–4341 (2014).

14. Abraham, D. P. *et al.* Microscopy and Spectroscopy of Lithium Nickel Oxide-Based Particles Used in High Power Lithium-Ion Cells. *J. Electrochem. Soc.* **150,** A1450 (2003).

15. Zheng, J. *et al.* Corrosion/Fragmentation of Layered Composite Cathode and Related Capacity/Voltage Fading during Cycling Process. *Nano Lett.* **13,** 3824–30 (2013).

16. Lin, M. *et al.* Insight into the Atomic Structure of High-Voltage Spinel LiNi 0.5 Mn 1.5 O 4 Cathode Material in the First Cycle. *Chem. Mater.* **27,** 292–303 (2015).

17. Qiao, R. *et al.* Direct evidence of gradient Mn(II) evolution at charged states in LiNi0.5Mn1.5O4 electrodes with capacity fading. *J. Power Sources* **273,** 1120–1126 (2015).

18. Jarry, A. *et al.* The formation mechanism of fluorescent metal complexes at the Li(x)Ni(0.5)Mn(1.5)O(4-δ)/carbonate ester electrolyte interface. *J. Am. Chem. Soc.* **137,** 3533–3539 (2015).

19. Markus, I. M., Lin, F., Kam, K. C., Asta, M. & Doeff, M. M. Computational and Experimental Investigation of Ti Substitution in Li 1 (Ni x Mn x Co 1–2 x – y Ti y)O 2 for Lithium Ion Batteries. *J. Phys. Chem. Lett.* **5,** 3649–3655 (2014).

20. Kam, K. C. & Doeff, M. M. Aliovalent titanium substitution in layered mixed Li Ni–Mn–Co oxides for lithium battery applications. *J. Mater. Chem.* **21,** 9991 (2011).

21. Kam, K. C., Mehta, A., Heron, J. T. & Doeff, M. M. Electrochemical and Physical Properties of Ti-Substituted Layered Nickel Manganese Cobalt Oxide (NMC) Cathode Materials. *J. Electrochem. Soc.* **159,** A1383–A1392 (2012).

22. Maier, J. Nanoionics: ion transport and electrochemical storage in confined systems. *Nat. Mater.* **4,** 805–815 (2005).

23. Nie, A. *et al.* Twin Boundary-Assisted Lithium Ion Transport. **15,** 610–615 (2015).

24. Cheng, L. *et al.* The origin of high electrolyte–electrode interfacial resistances in lithium cells containing garnet type solid electrolytes. *Phys. Chem. Chem. Phys.* **16,** 18294 (2014).

25. Cheng, L. *et al.* Effect of surface microstructure on electrochemical performance of garnet solid electrolytes. *ACS Appl. Mater. Interfaces* **7,** 2073–2081 (2015).

26. Belharouak, I., Lu, W., Vissers, D. & Amine, K. Safety characteristics of Li(Ni0.8Co0.15Al0.05)O2 and Li(Ni1/3Co1/3Mn1/3)O2. *Electrochem. commun.* **8,** 329–335 (2006).

27. Sun, Y.-K. *et al.* High-energy cathode material for long-life and safe lithium batteries. *Nat. Mater.* **8,** 320–324 (2009).

28. Sun, Y.-K. *et al.* Nanostructured high-energy cathode materials for advanced lithium batteries. *Nat. Mater.* **11,** 942–947 (2012).

29. Cho, Y., Oh, P. & Cho, J. A new type of protective surface layer for high-capacity ni-based cathode materials: Nanoscaled surface pillaring layer. *Nano Lett.* **13,** 1145–1152 (2013).

30. Jung, D. S., Ko, Y. N., Kang, Y. C. & Park, S. Bin. Recent progress in electrode materials produced by spray pyrolysis for next-generation lithium ion batteries. *Adv. Powder Technol.* **25,** 18–31 (2014).

31. Zhang, X. & Axelbaum, R. L. Spray Pyrolysis Synthesis of Mesoporous Lithium-Nickel-Manganese-Oxides for High Energy Li-Ion Batteries. *J. Electrochem. Soc.* **159,** A834 (2012).

32. Jung, D. S. *et al.* Hierarchical porous carbon by ultrasonic spray pyrolysis yields stable cycling in lithium-sulfur battery. *Nano Lett.* **14,** 4418–4425 (2014).

33. Bang, J. H., Didenko, Y. T., Helmich, R. J. & Suslick, K. S. Nanostructured Materials Through Ultrasonic Spray Pyrolysis. *Mater. Matters* **7,** 19–25 (2012).

34. Liu, J., Conry, T. E., Song, X., Doeff, M. M. & Richardson, T. J. Nanoporous spherical LiFePO4 for high performance cathodes. *Energy Environ. Sci.* **4,** 885 (2011).

35. Liu, J. *et al.* Spherical nanoporous LiCoPO4/C composites as high performance cathode materials for rechargeable lithium-ion batteries. *J. Mater. Chem.* **21,** 9984 (2011).

36. Kao, T. L. *et al.* Nanoscale elemental sensitivity study of Nd2Fe14B using absorption correlation tomography. *Microsc. Res. Tech.* **76,** 1112–1117 (2013).

37. Meirer, F. *et al.* Three-dimensional imaging of chemical phase transformations at the nanoscale with full-field transmission X-ray microscopy. *J. Synchrotron Radiat.* **18,** 773–781 (2011).

38. Wang, J., Chen-Wiegart, Y. K. & Wang, J. In operando tracking phase transformation evolution of lithium iron phosphate with hard X-ray microscopy. *Nat. Commun.* **5,** 4570 (2014).

39. Gu, M. *et al.* Conflicting roles of nickel in controlling cathode performance in lithium ion batteries. *Nano Lett.* **12,** 5186–91 (2012).

40. Zhou, L., Zhao, D. & Lou, X. LiNi(0.5)Mn(1.5)O4 hollow structures as high-performance cathodes for lithium-ion batteries. *Angew. Chem. Int. Ed. Engl.* **51,** 239–241 (2012).

41. Zhang, X. & Axelbaum, R. L. Spray Pyrolysis Synthesis of Mesoporous Lithium-Nickel-Manganese-Oxides for High Energy Li-Ion Batteries. *J. Electrochem. Soc.* **159,** A834 (2012).

42. Petersburg, C. F., Li, Z., Chernova, N. a., Whittingham, M. S. & Alamgir, F. M. Oxygen and transition metal involvement in the charge compensation mechanism of LiNi1/3Mn1/3Co1/3O2 cathodes. *J. Mater. Chem.* **22,** 19993 (2012).

43. Wilcox, J., Patoux, S. & Doeff, M. Structure and Electrochemistry of LiNi[sub 1⁄3]Co[sub 1⁄3−y]M[sub y]Mn[sub 1⁄3]O[sub 2] (M=Ti, Al, Fe) Positive Electrode Materials. *J. Electrochem. Soc.* **156,** A192 (2009).

44. Kang, S.-H., Yoon, W.-S., Nam, K.-W., Yang, X.-Q. & Abraham, D. P. Investigating the first-cycle irreversibility of lithium metal oxide cathodes for Li batteries. *J. Mater. Sci.* **43,** 4701–4706 (2008).

45. De Groot, F. M. F., Fuggle, J. C., Thole, B. T. & Sawatzky, G. a. 2p x-ray absorption of 3d transition-metal compounds: An atomic multiplet description including the crystal field. *Phys. Rev. B* **42,** 5459–5468 (1990).

46. Lin, F. *et al.* Hole doping in Al-containing nickel oxide materials to improve electrochromic performance. *ACS Appl. Mater. Interfaces* **5,** 301–9 (2013).

47. Lin, F. *et al.* Origin of electrochromism in high-performing nanocomposite nickel oxide. *ACS Appl. Mater. Interfaces* **5,** 3643–9 (2013).

48. Liu, W. *et al.* Nickel-rich layered lithium transition-metal oxide for high-energy lithium-ion batteries. *Angew. Chem. Int. Ed. Engl.* **54,** 4440–4457 (2015).

49. Liu, Y. *et al.* Phase retrieval using polychromatic illumination for transmission X-ray microscopy. *Opt. Express* **19,** 540–545 (2011).

50. Liu, Y. *et al.* TXM-Wizard: a program for advanced data collection and evaluation in full-field transmission X-ray microscopy. *J. Synchrotron Radiat.* **19,** 281–287 (2012).

Experimental Method

Materials synthesis The NMC materials were synthesized by spray pyrolysis followed by thermal annealing in a box furnace. The spray pyrolysis setup has been discussed in previous studies published by our group.[34,35] A 0.8 M (total transition metal ions) aqueous precursor solution containing metal nitrates with molar ratios of lithium, nickel, manganese and cobalt equal to 10.5: 4: 4: 2 was prepared. The solution was transferred to a syringe pump and delivered to an atomizer nozzle (Sonozap Model 120K50ST, 120 kHz) at a flow rate of 0.5 mL/min to generate microdroplets, which were then carried through a preheated quartz tube (700 °C) by air at a flow rate of 20 SCFH. The precursor microdroplets decomposed to form a powder and were collected at the end of the tube. This powder was then annealed in air for 6 hours with heating and cooling rates of 2 °C /min. A co-precipitation procedure described previously in references 10-12 was used to produce the sample shown in Figure 7.

Electrode preparation and electrochemical measurement Composite electrodes were prepared with 84 wt% active material, 8 wt% polyvinylidene fluoride (Kureha Chemical Ind. Co. Ltd), 4 wt% acetylene carbon black (Denka, 50% compressed) and 4wt% SFG-6 synthetic graphite (Timcal Ltd., Graphites and Technologies) in N-methyl-2-pyrrolidinone and cast onto carbon-coated aluminum current collectors (Exopack Advanced Coatings) with typical active material loadings of 2.0-2.5 mg/cm^2. 2032-type coin cells were assembled in an argon-filled glove box using the composite electrode as the positive electrode and Li metal as the negative electrode. A Celgard 2400 separator and 1 M $LiPF_6$ electrolyte solution in 1:1 v/v ethylene carbonate/diethyl carbonate (EC-DEC, Novolyte Technologies) were used in the coin cells. Battery testing was performed on a computer controlled VMP3 potentiostat/galvanostat (BioLogic). Galvanostatic cycling was performed at approximately C/20, where 1C was defined as fully charging a cathode in 1 h, corresponding to a specific current density of 280 mA/g. Each measurement was repeated to ensure the reproducibility of the electrochemical data. The electrodes were removed from coin cells,

rinsed with dimethyl carbonate and dried in an argon-filled glove box for further study. The electrodes were sealed under argon and then transferred to the synchrotron beamline using a homemade system to prevent air/moisture exposure. The samples were loaded into the vacuum chamber under Ar protection.

Materials Characterization X-ray Diffraction (XRD) on powder samples was performed on a Bruker D2 Phaser diffractometer using CuKα radiation. Scanning electron microscopy (SEM) was performed on a JEOL JSM-7000F with a Thermo Scientific Inc. EDS (energy dispersive x-ray spectroscopy) detector. X-ray absorption spectroscopy (XAS) measurements were performed on the 31-pole wiggler beamline 10-1 at Stanford Synchrotron Radiation Lightsource (SSRL) using a ring current of 350 mA and a 1000 $l \cdot mm^{-1}$ spherical grating monochromator with 20 μm entrance and exit slits, providing ~10^{11} $ph \cdot s^{-1}$ at 0.2 eV resolution in a 1 mm^2 beam spot. During the measurements, all battery electrode samples were attached to an aluminum sample holder using conductive carbon tape (X-ray beam probing the top surface of the composite electrodes). Data were acquired under ultrahigh vacuum (10^{-9} Torr) in a single load at room temperature using total electron yield mode (TEY). The sample drain current was collected for TEY. All spectra were normalized by the current from freshly evaporated gold on a fine grid positioned upstream of the main chamber. The transmission X-ray microscopy was performed at beamline 6-2c of the SSRL. The details of the experimental setup can be found in a previous publication.[49] The samples were loaded in quartz capillaries enabling full rotation from -90° to 90° with angular step size at 1°. Slow and steady helium flow was applied to the samples to reduce the radiation-induced heat load on the sample in the tomography scans. X-ray nano-tomography was performed at 6 different energies (6530 eV, 6550 eV, 7700 eV, 7720 eV, 8324 eV, and 8344 eV) above and below the K-edges of the three transition metal elements (Mn, Co, and Ni) in order to resolve the elemental distribution. The tomographic reconstruction, which results in effective 3D voxel size at 32.5×32.5×32.5 nm^3 (spatial resolution), and the analysis of the elemental association[36] were performed using an in-house developed software package known as TXM-Wizard.[50] Two probe-corrected field-emission scanning transmission electron microscopes (STEM) operated at 200 keV and 300 keV were used for annular dark-field STEM (ADF-STEM) imaging and spatially resolved electron energy loss spectroscopy (EELS).

Acknowledgement

This work was supported by the Assistant Secretary for Energy Efficiency and Renewable Energy, Office of Vehicle Technologies of the U.S. Department of Energy under Contract No. DE-AC02-05CH11231. This research used the Hitachi dedicated STEM of the Center for Functional Nanomaterials, which is a U.S. Department of Energy Office of Science Facility, at Brookhaven National Laboratory under Contract No. DE-SC0012704. The synchrotron X-ray portions of this research were carried out at the Stanford Synchrotron Radiation Lightsource, a Directorate of SLAC National Accelerator Laboratory and an

Office of Science User Facility operated for the U.S. Department of Energy Office of Science by Stanford University. Use of the Stanford Synchrotron Radiation Lightsource, SLAC National Accelerator Laboratory, is supported by the U.S. Department of Energy, Office of Science, Office of Basic Energy Sciences under Contract No. DE-AC02-76SF00515. F.L., D.N. and T.-C.W. would like to thank Dr. J.-S. Lee and G. Kerr for their assistance at SSRL.

Author contributions

F.L., Y.Liu, H.L.X. and M.M.D. participated in conceiving and designing the experiments. F.L. performed the materials syntheses, electrochemical measurements and characterization, and wrote the paper with assistance from M.M.D, Y.Liu, and H.L.X. F.L., Y.Liu, D.N. and T.-C.W designed and performed synchrotron experiments. Y.Liu analyzed the TXM tomography data. H.L.X. performed STEM-EELS experiments and co-analyzed the data with F.L. Y.Li and M.K.Q. participated in developing materials syntheses. L.C. participated in the data analysis and discussion. M.M.D supervised the project. All authors participated in discussions and know the implications of the work.

Additional information

Supplementary Information accompanies this paper at http://www.nature.com/nenergy

Competing financial interests: The authors declare no competing financial interests.

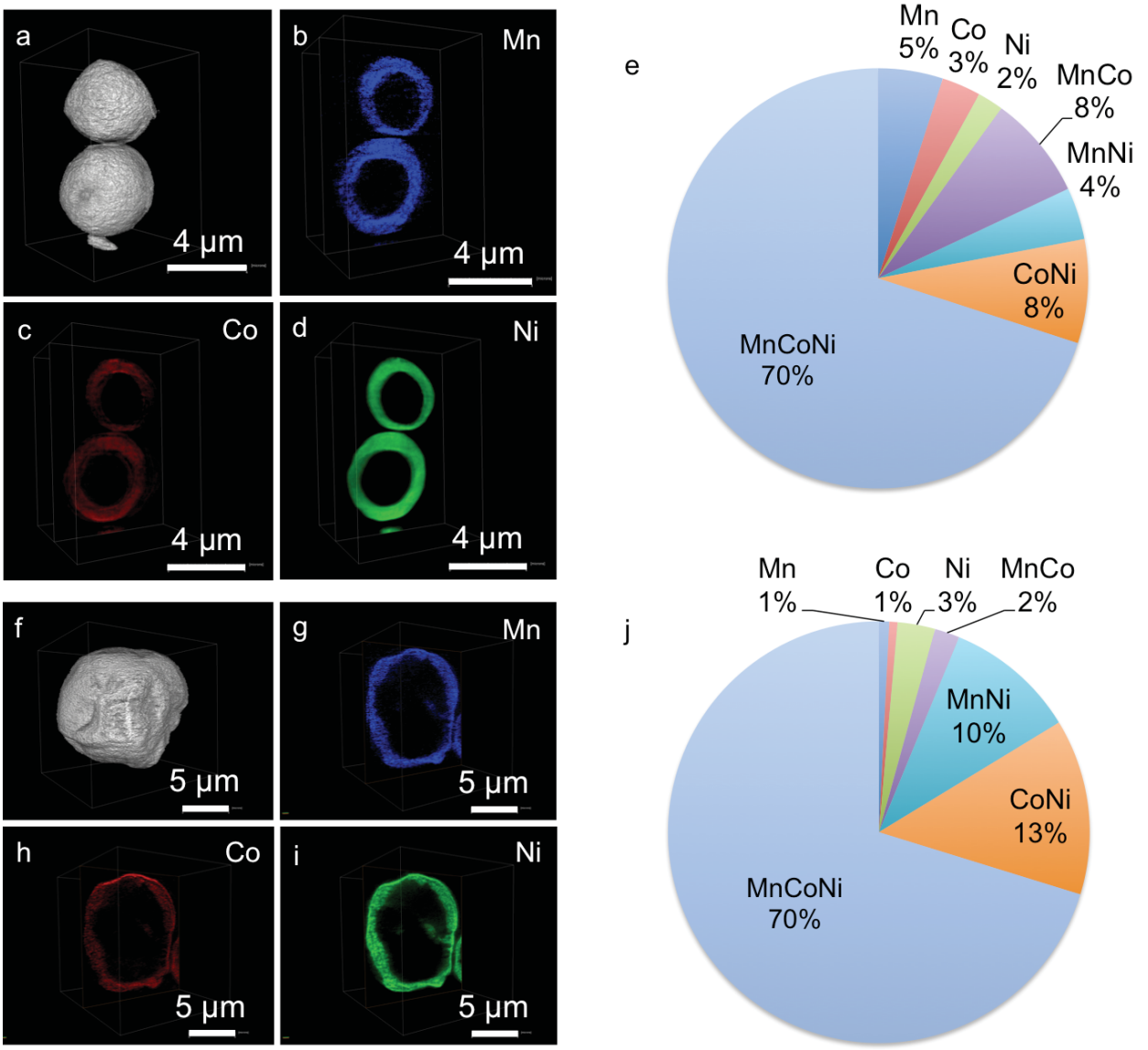

Figure 1. Elemental mapping and association calculation using transmission X-ray tomography. 3D elemental distribution of selected NMC particles collected (a) directly after spray pyrolysis and (b) after subsequent annealing at 850 ºC. (i) Single energy tomography provides 3D morphology of the particles, (ii-iv) multi-energy tomography data with elemental sensitivity, visualized by slicing through the center of the particles, with the blue, red and green representing Mn, Co and Ni, respectively and (v) the relative concentrations of 3D elemental associations calculated by using absorption correlation tomography. Movies of 3D elemental distributions are shown in Movies 1 and 2 in the Supporting Information.

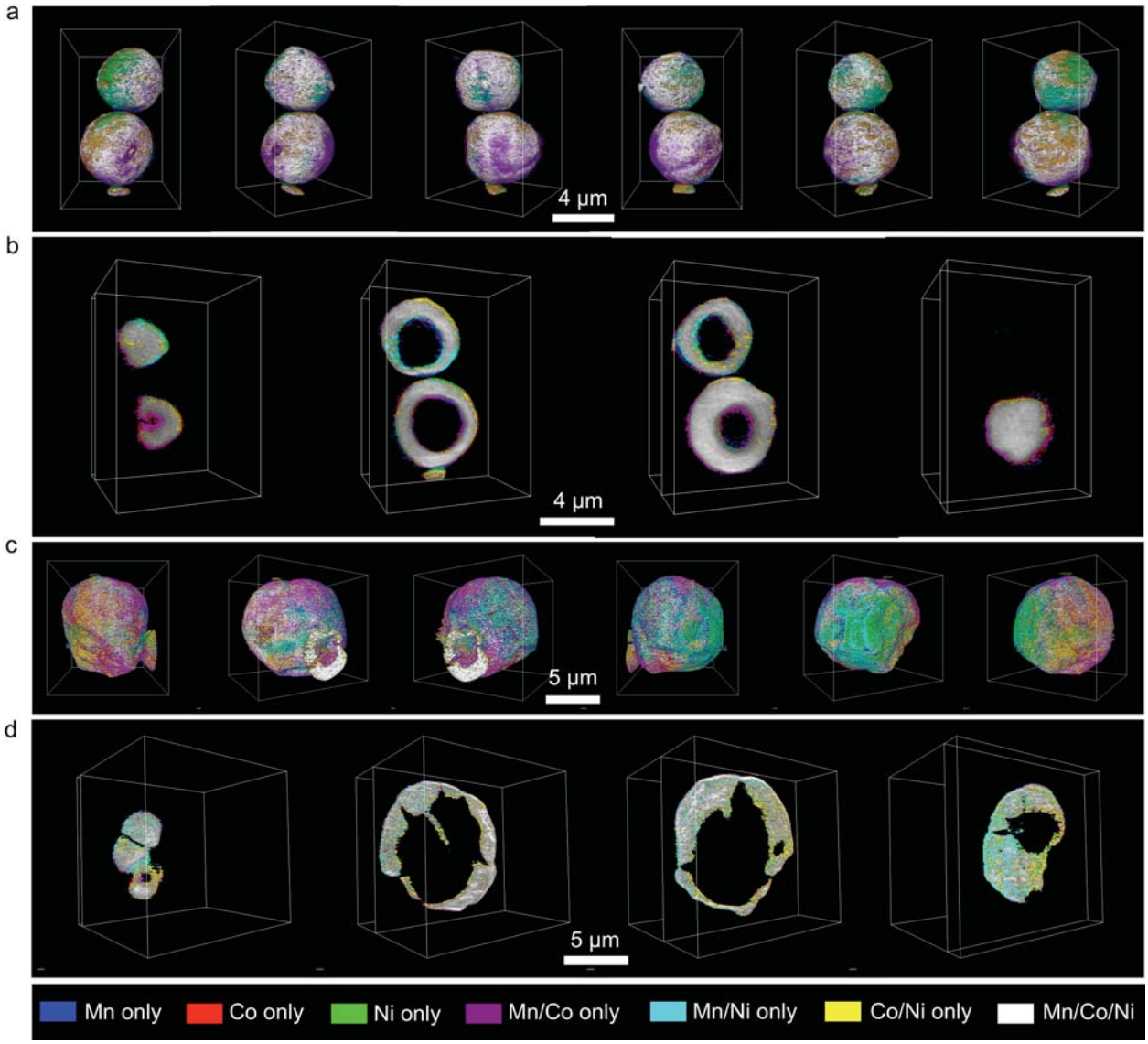

Figure 2. 3D elemental association maps generated using transmission X-ray tomography. Elemental association maps of (a, b) the as-made NMC precursor after spray pyrolysis and (c, d) the powder after annealing at 850 ºC. (a, c) 3D rendering of the elemental associations viewing the particles at different angles. (b, d) 2D slices of the elemental associations. The colors presenting the elemental associations are shown at the bottom.

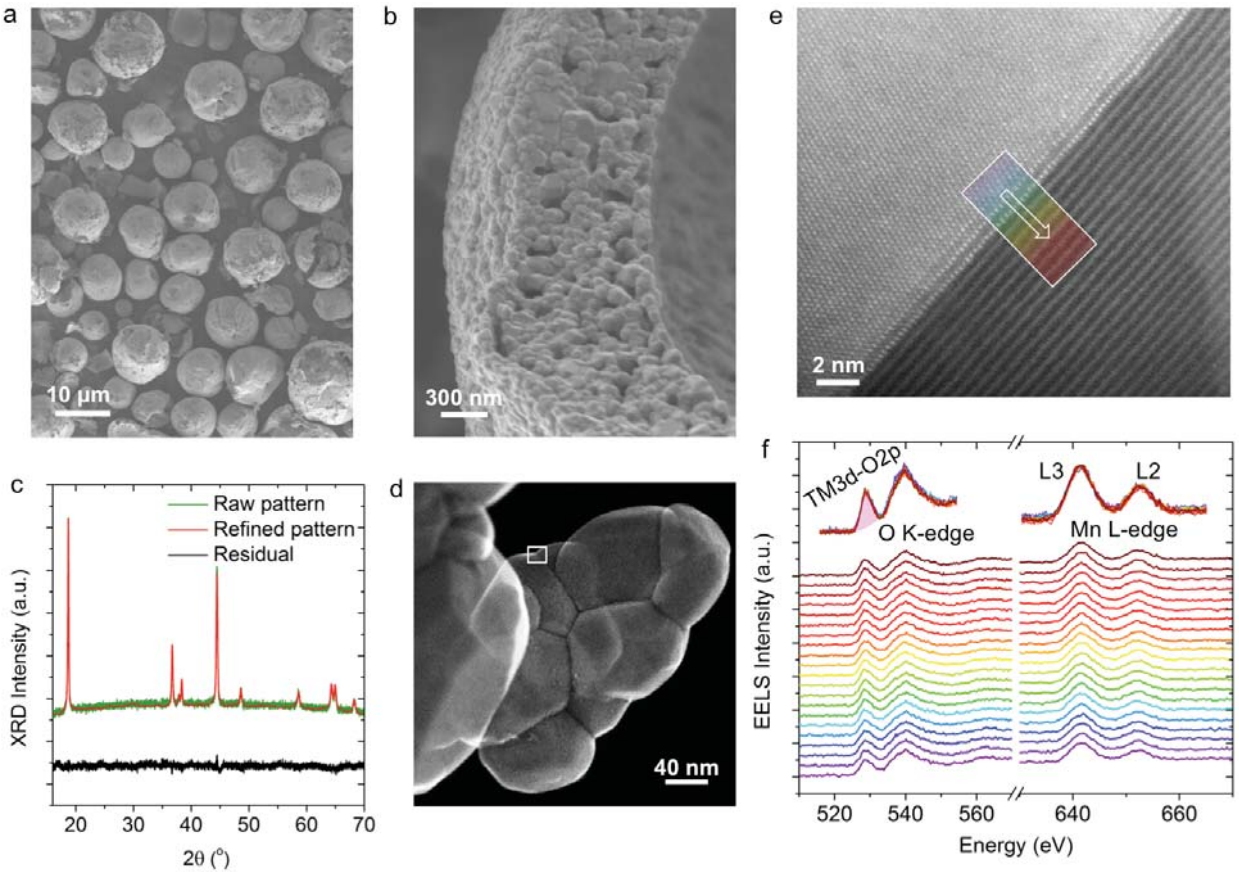

Figure 3. **Characterization of the NMC-442 materials synthesized by spray pyrolysis.** (a-b) SEM at different magnifications, (c) XRD and Rietveld refinement, and (d-e) SEM-STEM-EELS, where a selected particle-particle interface marked in (d) was used for (e) ADF-STEM imaging and (f) EELS O K-edge and Mn L-edge measurements. In the brighter particle (left) in (e), two domains that are π out of phase are projected in this image.

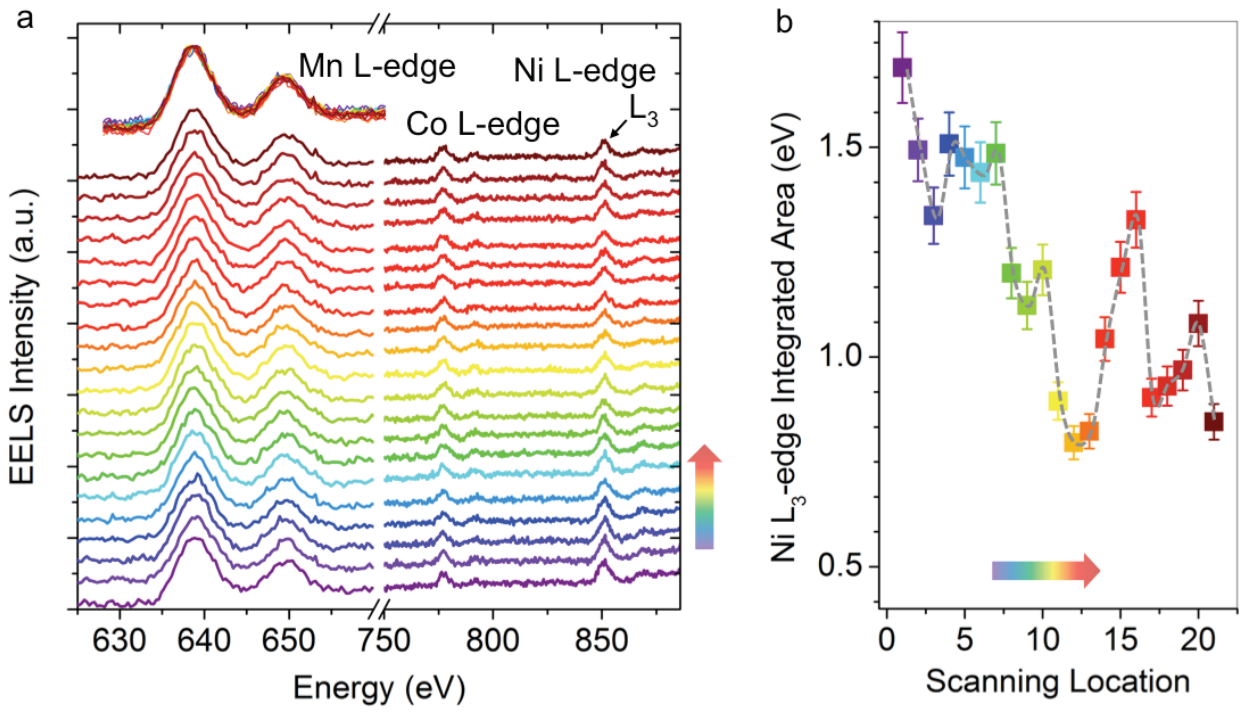

Figure 4. **Electronic and compositional characterization using EELS.** (a) Transition metal L-edge EELS spectra along the scanning pathway shown in Figure 3e, where the spectra were normalized using Mn L-edge. The normalized spectra were overlapped on the top of the stacked spectra, demonstrating the identical peak characteristics for all the Mn L-edge spectra. The Ni L_3-integrated areas were calculated after the Mn L-edge normalization and plotted in (b). The colored arrows in the figure represent the scanning direction corresponding to the one in Figure 3e.

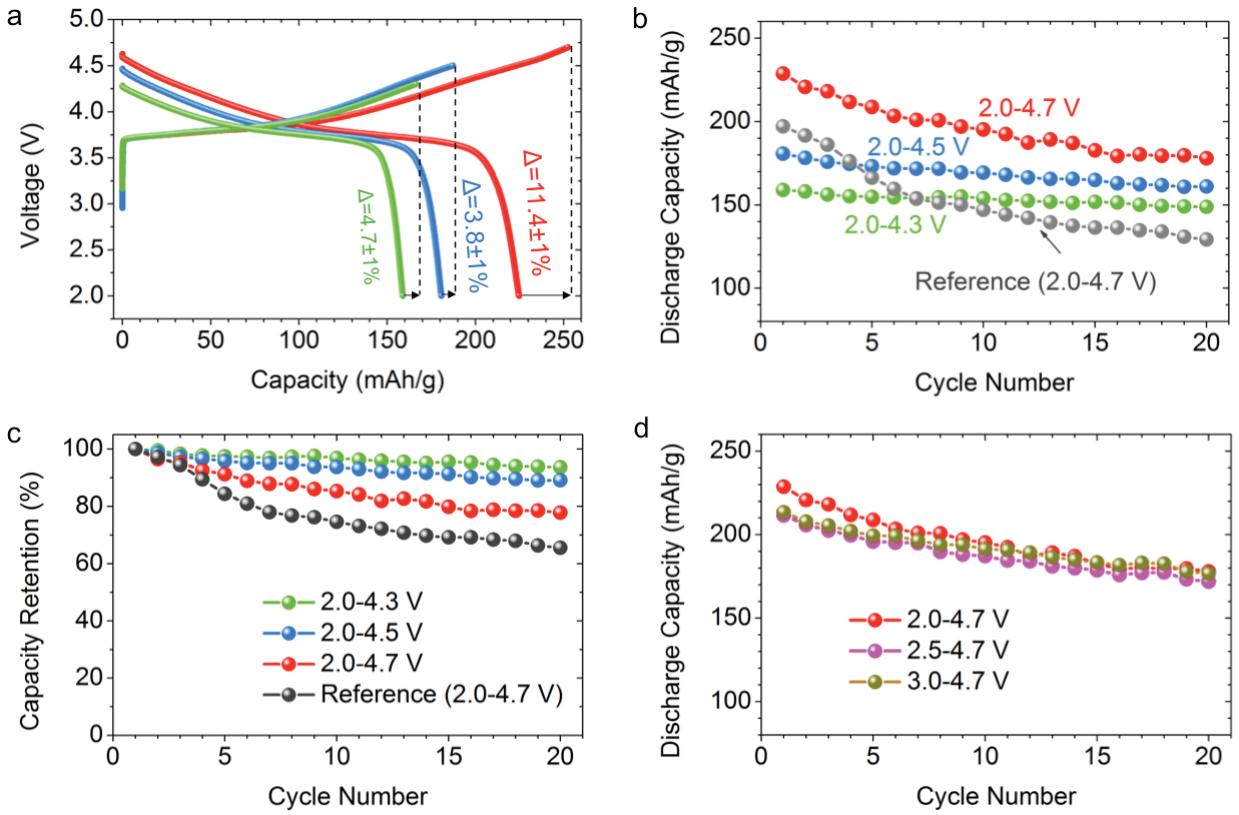

Figure 5. **Battery cycling performance of lithium half-cells containing the NMC-442 materials.** (a) First charge-discharge cycles between various voltage cutoff windows with % Coulombic inefficiencies indicated. Red, blue and green lines represent voltage limits of 2.0-4.7 V, 2.0-4.5 V and 2.0-4.3 V, respectively. The cells were cycled at approximately similar rates. (b) Discharge capacities as a function of cycle numbers during the galvanostatic cycling, with reference data taken from[21] on an NMC-442 material prepared by a glycine-nitrate combustion method and cycled between 2.0-4.7 V. (c) Discharge capacity retention at various cutoff voltages during 20 cycles. (d) Discharge capacity as functions of cycle number and cutoff voltages. All cells were cycled at approximately C/20 and an extra amount of electrolyte was added in coin cells to isolate the effects of electrolyte oxidation (e.g., electrolyte deficiency).

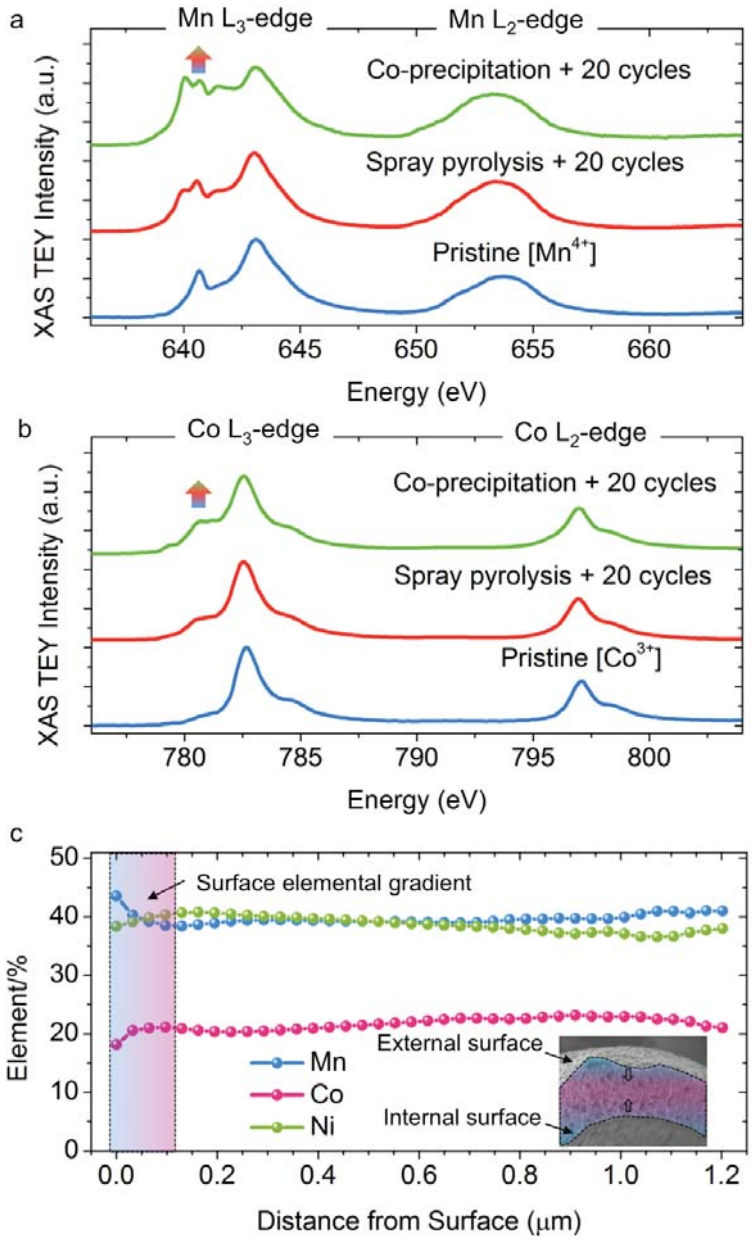

Figure 6. **Surface chemistry of NMC materials before and after electrochemical cycling.** XAS spectra of (a) Mn L-edge and (b) Co L-edge of NMCs in the pristine state (blue) and after 20 charge-discharge cycles to 4.7 V *vs* Li/Li^+ (red and green), stopped in the discharged state. Transition metal L-edges are divided into L_3 and L_2 features located at lower and higher energy regions of the spectra, respectively. The co-precipitation data is used with permission from reference 11. (c) Elemental distribution as a function of the distance from microsphere surface calculated using the TXM data, and the elemental distribution at the surface region is highlighted using the light-blue shadow. The distance from surface was calculated from both the internal and external surfaces of the hollow shell, as schematically shown in the inset.

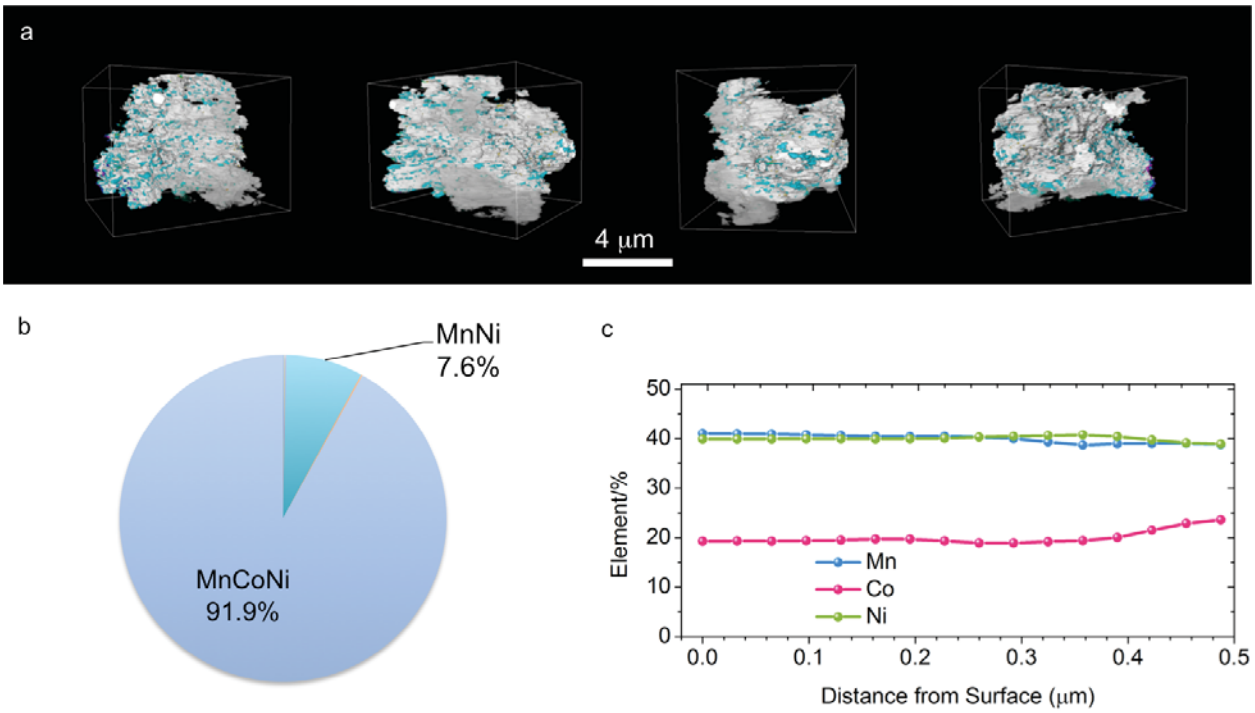

Figure 7. **3D elemental association mapping and elemental distribution of co-precipitated NMC particles using transmission X-ray tomography** (a) Elemental association maps of a particle selected from the co-precipitated sample, where the cyan color represents the regions where Co was not observed. (b) The relative concentrations of 3D elemental associations calculated by using absorption correlation tomography, elemental associations other than MnCoNi and MnNi were all below 1%. (c) Elemental distribution as a function of the distance from secondary particle surface calculated using the TXM data, in direct comparison with Figure 6c.

Supporting Information for

Metal Segregation in Hierarchically Structured Cathode Materials for High Energy Lithium Batteries

Feng Lin,[1] Dennis Nordlund,[2] Yuyi Li,[1] Matthew K. Quan,[1] Lei Cheng,[1,3] Tsu-Chien Weng,[2,†] Yijin Liu,[2,*] Huolin L. Xin[4,*] & Marca M. Doeff[1,*]

1. Energy Storage and Distributed Resources Division, Lawrence Berkeley National Laboratory, Berkeley, CA 94720, USA
2. Stanford Synchrotron Radiation Lightsource, SLAC National Accelerator Laboratory, Menlo Park, CA 94025, USA
3. Department of Materials Science and Engineering, University of California, Berkeley, CA 94720, USA
4. Center for Functional Nanomaterials, Brookhaven National Laboratory, Upton, NY 11973, USA

† Present address: Center for High Pressure Science & Technology Advanced Research, Shanghai 201203, China

Corresponding authors

Y.Liu liuyijin@slac.stanford.edu **H.L.X.** hxin@bnl.gov **M.M.D.** mmdoeff@lbl.gov

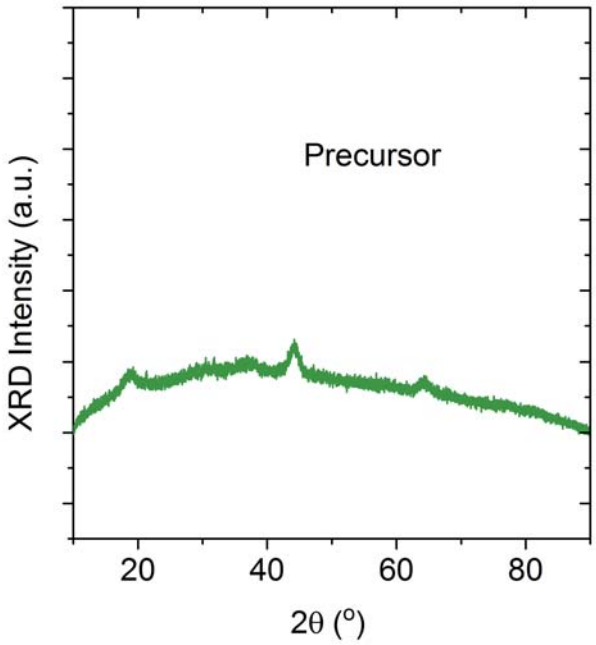

Figure S1. Crystal structure of the NMC-442 precursor powder. XRD pattern for the precursor powder collected after spray pyrolysis, prior to the thermal annealing at 850 ºC.

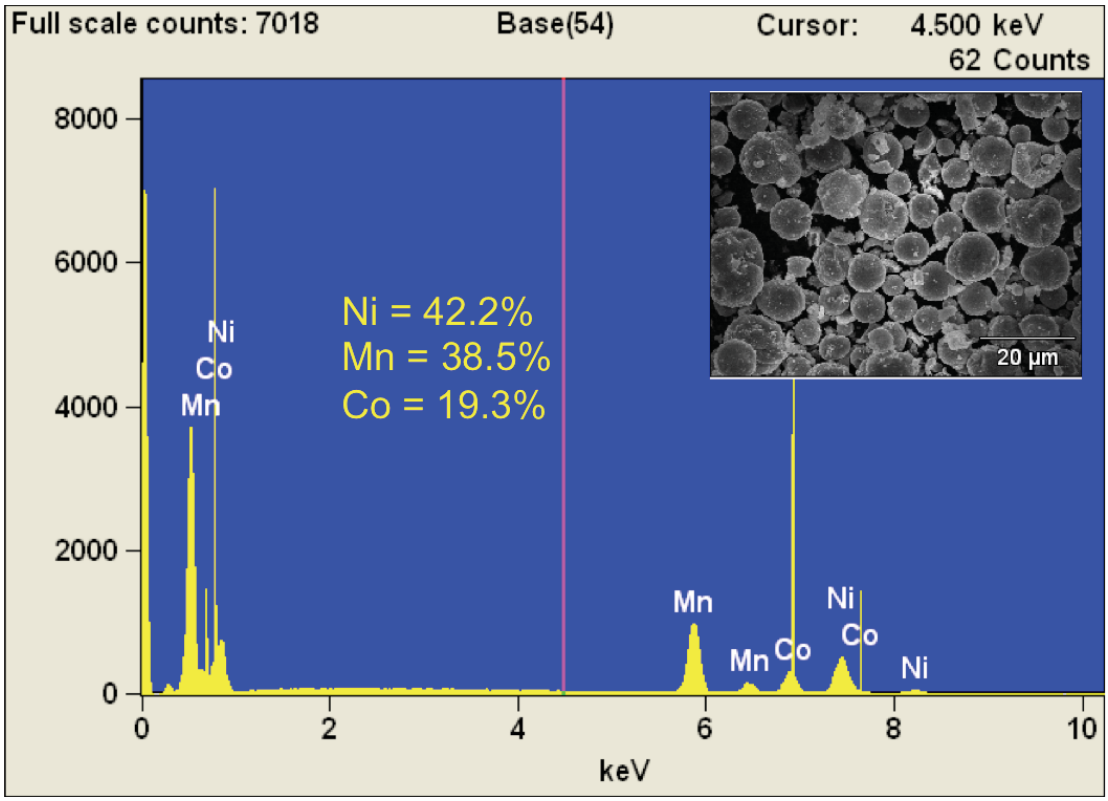

Figure S2. Compositional characterization of the spray-pyrolyzed NMC-442 materials. EDS quantification of transition metal percentages in the resulting NMC-442 materials, where the spectrum was collected from the large area shown in the SEM image (inset). The experimental error of EDS quantification is approximately ±2%.

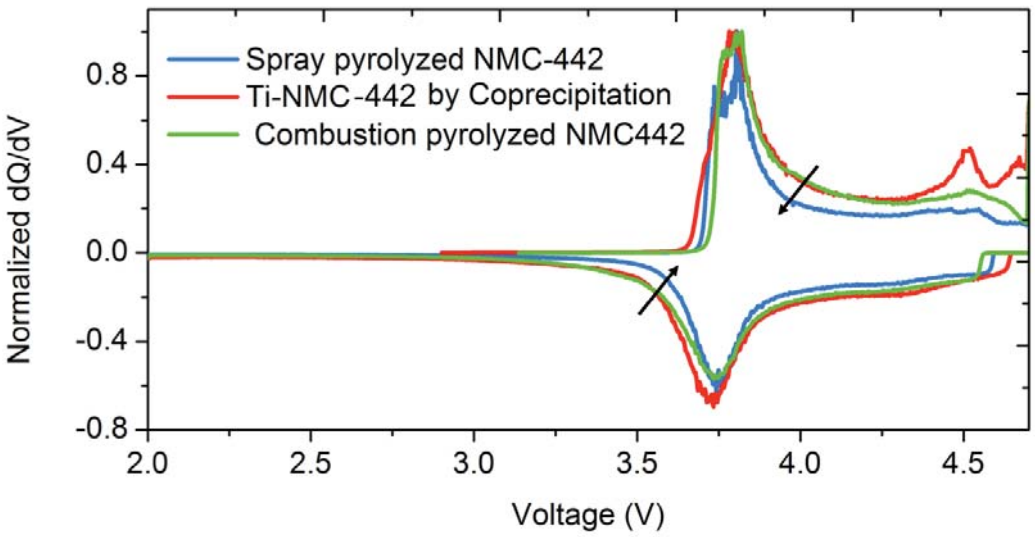

Figure S3. Differential capacity plots of the first cycles of lithium half-cells containing NMC materials. The cell containing spray pyrolyzed NMC-442 material (blue) shows less polarization than those containing co-precipitated Ti-substituted NMC-442 (red) and combustion synthesized NMC-442 (green) materials.